

In situ synchrotron tomographic quantification of granular and intragranular deformation during semi-solid compression of an equiaxed dendritic Al–Cu alloy

B. Cai^{a,b}, S. Karagadde^{a,b}, L. Yuan^c, T.J. Marrow^d, T. Connolley^e, P.D. Lee^{a,b,*}

^a School of Materials, University of Manchester, Manchester, UK

^b Research Complex at Harwell, Rutherford Appleton Laboratory, Harwell, Oxfordshire, UK

^c GE Global Research Center, Niskayuna, NY, USA

^d Department of Materials, University of Oxford, Oxford, UK

^e Diamond Light Source Ltd., Harwell Science and Innovation Campus, Didcot, UK

Received 17 April 2014; received in revised form 10 May 2014; accepted 16 May 2014

Abstract

Semi-solid deformation mechanisms are important in a range of manufacturing and natural phenomena, which range from squeeze casting to magma flows. Using fast synchrotron X-ray tomography and a bespoke precision thermomechanical rig, we performed a four-dimensional (3-D plus time) quantitative investigation of the granular behaviour of equiaxed dendritic three-phase materials. This methodology produced new insights into the formation of damage during the isothermal semi-solid compression (~30% liquid fraction) of an Al–15 wt.%Cu alloy at both a macroscopic and microscopic level. Grain rearrangements, such as translation and rotation, were observed and lead to local dilatancy. The resulting flow of Cu-rich intergranular liquid into the dilated interstices gave rise to a local increase in liquid fraction, followed by rapid void growth above a critical axial strain of –6.4%. The local normal and shear strain distributions were quantified using digital volume correlation, identifying dilatant shear bands. At a microstructural level, the individual grains were also seen to undergo intragranular deformation, leading to bending and fragmentation of dendrites as grains interlock.

© 2014 Acta Materialia Inc. Published by Elsevier Ltd. This is an open access article under the CC BY license (<http://creativecommons.org/licenses/by/3.0/>).

Keywords: Semi-solid deformation; Granular mechanics; Microstructural response; Dilatancy; Hot tearing

1. Introduction

The microstructural and mechanical response of semi-solid mixtures in the range of 20–50% liquid fraction during deformation is termed semi-solid mechanics. This range of liquid fraction is important in both materials processing (e.g. metallic component fabrication [1,2]) and many natural phenomena (e.g. magma flows [3,4]). For example,

during the casting of aerospace or automotive metallic components, the thermal contraction and/or imposed deformation during solidification can influence the microstructure and defects formed (e.g. grain size [5], porosity [6], segregation [7] and hot tearing [1,8]). In many industrial processes where deformation is imposed, such as semi-solid processing and twin roll casting, the effect is particularly strong [5,9]. Therefore, an improved understanding of the response of a solidifying structure to deformation is important when designing a range of manufacturing processes.

Semi-solid systems are conventionally treated as homogeneous media, described using governing laws based on a continuum approach [10,11]. However, this treatment

* Corresponding author at: School of Materials, University of Manchester, Manchester, UK.

E-mail addresses: peter.lee@manchester.ac.uk, p.d.lee@ic.ac.uk (P.D. Lee).

cannot account for localized phenomena, such as strain localization, which leads to defects such as shear banding or void formation [12]. A granular mechanics approach has been proposed by some authors to link the microstructural evolution to the semi-solid responses due to deformation, by treating solid grains as particulate suspensions [5,12–15]. For example, Spencer et al. [13] discovered that a semi-solid metallic alloy's viscosity depends on the solid fraction and decreases with increasing shear rate (shear-thinning), analogous to colloidal suspensions. Tzimas and Zavaliangos [16] discussed the occurrence of dilatancy in semi-solid equiaxed alloys during compression, and more recently Gourlay et al. [2] reported that partially solidified alloys exhibit Reynolds dilatancy under shear leading to strain localization. Dilation is also an important feature of saturated granular materials. The previous studies suggest that the size and morphology of solid particles and the liquid fraction influence the occurrence of granular phenomena in semi-solid alloys [17,18]. Although granular mechanics can explain some features observed during the deformation of three-phase solids, many other behaviours have been observed in such systems that are not currently explained by these models, such as grain-to-grain interactions and liquid flow, and the resulting localized phenomena at a microstructural scale, such as flow of solid particles [19,20] agglomeration/deagglomeration [9,21], viscoplastic deformation of grains [1,22,23] and damage formation [24–26]. Whether such behaviour can be explained by granular mechanics needs to be validated through experiments.

Commonly, constitutive equations have been used to describe the mechanical behaviour of semi-solid alloys via continuum analysis of a range of tests, including: tensile loading [26–29], compression [30–32], direct shear [33], rheometry [13,17,34] and indentation [35]. It is worth noting here that compression has been extensively used due to its ease of implementation and close resemblance to many key industrial processes. Additionally, properties such as the yield stress and viscosity of a semi-solid mush can be directly measured [30–32]. However, in most of these studies, the effects of deformation on microstructure were quantified only using post mortem analysis, limiting our understanding of any time-dependent kinetics. To understand and quantify the underlying kinetics or microstructure-dependent interactions, simultaneous measurement of the mechanical properties of semi-solid alloys and direct quantification of microstructural evolution with time is necessary.

A few recent studies have reported direct observation of granular shear deformation in semi-solid Al–15 wt.%Cu alloys [19] and low-carbon steel [36] using X-ray radiography, but did not measure the macroscopic mechanical behaviour. However, these 2-D studies did provide the first direct evidence of local dilatancy, induced by rearrangement of grains under shear deformation in metallic systems [19,37,38]. Unfortunately, these radiographic observations require a very thin sample thickness, and may not represent

the 3-D bulk behaviour due to restricted out-of-plane motion and the friction of particles along the sample container wall.

Ultra-fast X-ray tomography can now overcome many of the limitations of radiography, resolving real-time 4-D information [39–42]. This technique has been used by several authors to quantify microstructure and defect formation during solidification [43–45] and under tension [8,46,47]. In this study, we present the first in situ 4-D (3-D plus time) quantitation of semi-solid compression of equiaxed dendritic grains. Using a bespoke thermomechanical rig designed for X-ray tomography, both the macroscopic mechanical behaviour and the evolution of microstructure and damage are simultaneously measured. The microstructural dynamics can then be correlated with the true stress and strain measurements, providing fundamental understanding of the responses of partially solidified alloys to the imposed loading. We demonstrate that this methodology can provide unique advantages when developing and validating semi-solid constitutive models, elucidating the behaviour of granular semi-solid systems and the nature of underlying granular deformation mechanisms.

2. Experimental methods

2.1. Materials

An Al–15 wt.%Cu alloy was selected for two key reasons: firstly to achieve a solid fraction typical of widely used commercial alloys (e.g. A356 [48]); and secondly for its X-ray attenuation variation between the primary phase and interdendritic liquid. The latter is due to the higher electron density of copper and its low partition coefficient, resulting in preferential segregation into the interdendritic liquid. Cylinders 3 mm diameter and 4 mm high were wire electrodischarge machined from 2 kg cast cylinders. Their microstructure was equiaxed dendritic, with a grain size of $\sim 600 \mu\text{m}$.

2.2. Testing apparatus and procedures

Semi-solid compression tests were performed using the bespoke P2R mechanical test rig [8] designed for in situ X-ray tomographic experiments, with air-bearing continuous rotation built into the load train. This allows simultaneous tension, compression and/or torsion during tomography, with 100 nm motion and 0.1 N load measurement precision. A bespoke PID-controlled resistance furnace with an X-ray-transparent window [8,41,49] was mounted on the mechanical rig, and the entire thermomechanical setup was integrated into the I12 beamline at Diamond Light Source (Fig. 1a).

The experimental setup is shown in the insert of Fig. 1a. The specimen was placed at the centre of a boron nitride holder (inner diameter 7 mm, wall thickness 1 mm) to ensure that the sample was secure and the deformation was unconstrained. A pre-load of 3 N was applied to

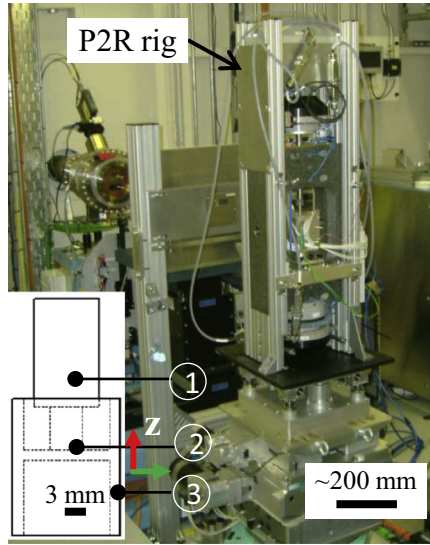


Fig. 1. Picture of P2R compression rig at the I12 beamline in Diamond Light Source with furnace; the insert shows a schematic of the setup: (1) compression (top) ram; (2) specimen; (3) boron nitride holder.

stabilize the sample during rotation for tomography. The specimen was heated at a rate of $40\text{ }^{\circ}\text{C min}^{-1}$ to $555 \pm 2\text{ }^{\circ}\text{C}$, where it is semi-solid with a liquid fraction of $30\% \pm 2\%$, and held isothermally for 10 min during which slight coarsening occurred. (Note: the liquid fraction was determined by image analysis of tomographic scans, but compares well with the equilibrium phase diagram.) The sample was then compressed at a displacement rate of $5\text{ }\mu\text{m s}^{-1}$ (an initial strain rate of $\sim 1.25 \times 10^{-3}\text{ s}^{-1}$). After 20 s, continuous fast X-ray tomographic imaging was initiated, and 24 datasets were continuously captured over 96 s (i.e. one tomogram every 4 s of 720 images collected over 180°).

A monochromatic X-ray beam with photon energy of 53 keV was used in the experiment. A Phantom V7.3

high-speed camera (Vision Research, USA), together with a LuAg:Ce single-crystal scintillator was used, offering a field of view of $9.8 \times 7.3\text{ mm}^2$ and a voxel size of $12.25\text{ }\mu\text{m}$; the exposure time was 5.5 ms.

2.3. 3-D image reconstruction and quantification

A filtered back-projection algorithm was used to reconstruct the 3-D tomographic datasets, including ring artefact removal [50]. Each reconstructed 3-D dataset was $800 \times 600 \times 600$ pixels. Image processing and analysis was performed using Avizo 7.0.1 (Visualization Science Group, France), ImageJ (US NIH, Bethesda, MD, USA) [51] and MATLAB2012b (Mathworks Inc., USA). The first stage was a 3-D median filter algorithm to reduce noise, followed by registration using a 3-D affine registration approach. A longitudinal section of an individual tomogram is shown in Fig. 2a, where the α -Al dendrites are dark grey, and the Cu-enriched interdendritic liquid is light grey. Global thresholding was used to segment the images into solid, liquid and void. Voids smaller than 27 voxels were discounted as noise. The local thickness of the liquid channel was determined using BoneJ, an ImageJ plugin [52].

The length (l_i , where i is the scan step), maximum cross-section area (A_i) and volume (V_i) of the sample were measured from the 3-D tomographic volume, and used to calculate the true axial ($\epsilon_l = \ln(\frac{l_i}{l_0})$) and lateral ($\epsilon_a = \ln(\frac{A_i}{A_0})$) strains.

2.4. Digital volume correlation

Digital volume correlation (DVC; Davis Strain Master, version 8.1), was used to provide a full-field displacement field and 3-D strain map. DVC tracks intensity patterns within small subvolumes in a digital 3-D image, calculating their motion between frames, and hence displacements and

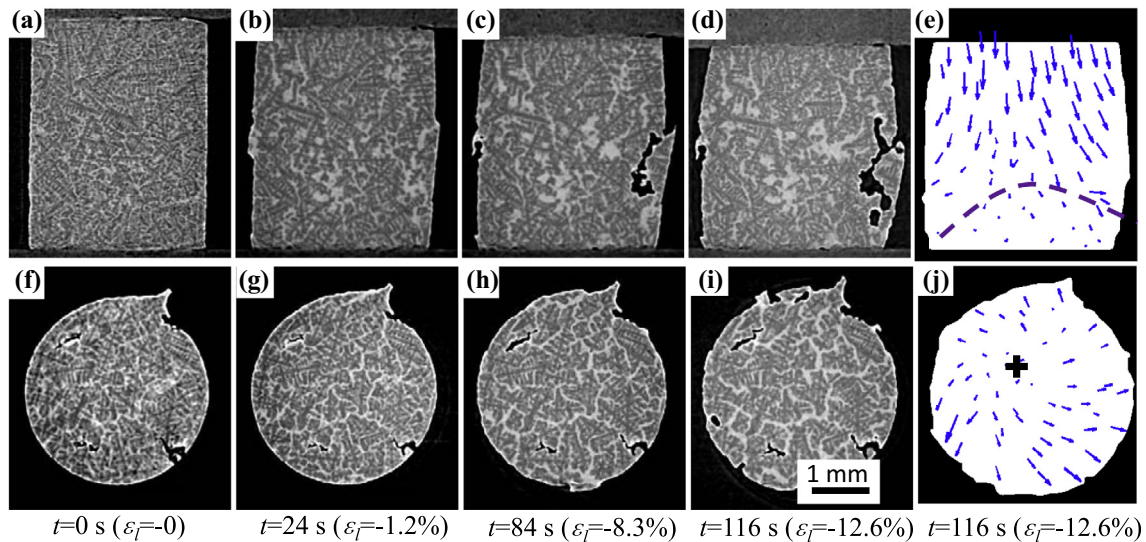


Fig. 2. (a)–(d) Series of longitudinal slices from 3-D volume of semi-solid Al-15 wt.%Cu alloy with liquid fraction of $30\% \pm 2\%$ under semi-solid compression; (f)–(i) mid-height transverse slices; (e) and (j) grain displacement from $\epsilon_l = -1.2\%$ to $\epsilon_l = -12.6\%$ (the dashed line indicates the discontinuity of displacement field, “+” shows the central point of displacement field).

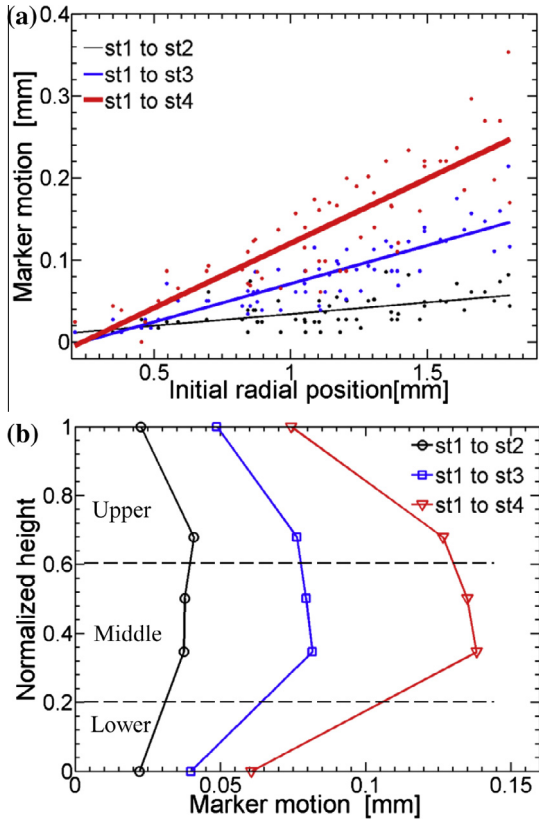


Fig. 3. (a) Grain motion in the transverse mid-height section; (b) average radial marker displacement vs. height (st1 at $t = 24$ s ($\epsilon_l = -1.2\%$), st2 at $t = 52$ s ($\epsilon_l = -4.2\%$), st3 at $t = 84$ s ($\epsilon_l = -8.3\%$) and st4 at $t = 116$ s ($\epsilon_l = -12.6\%$)).

strains [53]. Cuboidal subvolumes with an edge length of 24 pixels were chosen as a balance between being large enough to contain a unique pattern for matching, whilst being small enough to avoid affine straining over a deformation increment [54]. Using a 50% overlap and four passes, a displacement matrix grid of 12 pixels or $147 \mu\text{m}$ was obtained. The displacement field (V_i ($i = x, y, z$)) was used to calculate the strain tensor (ϵ_{ij} ($i, j = x, y, z$)); the coordinates are displayed in Fig. 1, z being the vertical axis in the direction of loading. The six unique components of ϵ_{ij} define the 3-D strain state, and can be transformed onto the octahedral planes, which are the eight planes forming equal angles with each of the principal strain directions, resulting in the octahedral normal strain (ϵ_n):

$$\epsilon_n = \frac{1}{3}(\epsilon_{xx} + \epsilon_{yy} + \epsilon_{zz}) \quad (1)$$

and the octahedral shear strain (ϵ_s):

$$\epsilon_s = \frac{2}{3} \sqrt{(\epsilon_{xx} - \epsilon_{yy})^2 + (\epsilon_{xx} - \epsilon_{zz})^2 + (\epsilon_{yy} - \epsilon_{zz})^2 + 6(\epsilon_{xy}^2 + \epsilon_{xz}^2 + \epsilon_{yz}^2)} \quad (2)$$

ϵ_n describes the volume change, equivalent to three times the volumetric strain, while ϵ_s is the maximum value of the shear strain on any plane. Both components are independent of the orientation of the coordinate system.

3. Results and discussion

3.1. Dilation during semi-solid compression

Initially (Fig. 2a and f), there is a uniform distribution of interdendritic liquid throughout the sample with only minor microstructural variations. As compression proceeds ($\epsilon_l = -1.2\%$), the sample shows typical barrelling (Fig. 2b) due to friction at the platens. Near the centre the α -Al equiaxed dendritic grains separate (Fig. 2c and d), drawing interdendritic liquid into that region and increasing the local liquid fraction (Fig. 2f and g). We also observe void nucleation and growth with increasing strain, showing the complex, heterogeneous interaction and deformation of the three phases (solid dendritic grains, interdendritic liquid and voids) under compression.

Grain movement during semi-solid compression can be quantified using markers at the grain centroids and dendrite tips. The marker motion was quantified at axial strain intervals of $\sim 4\%$ in longitudinal and transverse slices using the bottom ram as the frame of reference (Fig. 2e and j). Grains just below the top ram (upper part) move vertically downward, while grains in the middle region move simultaneously downwards and outwards. The motion in a single transverse mid-height plane is plotted in Fig. 3a and the radial motion at the central plane in Fig. 3b. As grains move, they also undergo small rotations.

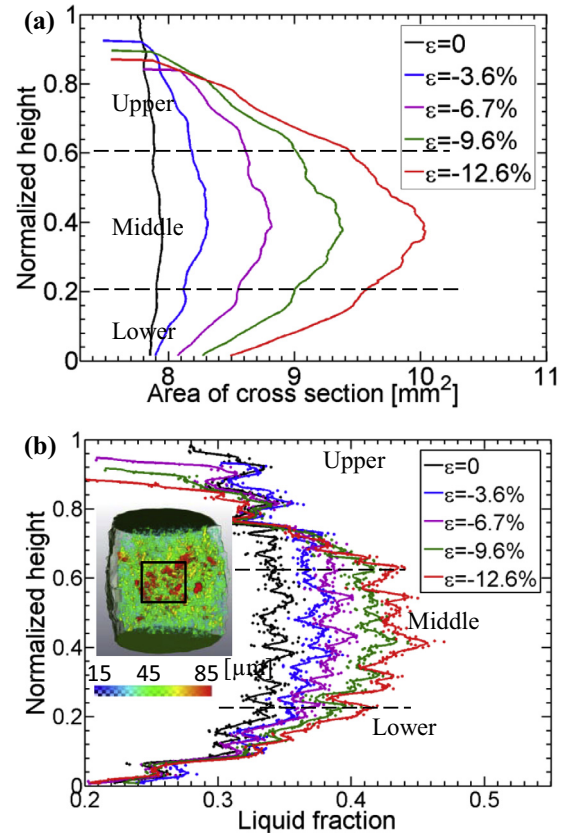


Fig. 4. (a) Variation in transverse cross-sectional area; (b) variation of area liquid fraction (line-weighted average) along deformation axis. Insert: the 3-D rendering of liquid channel thickness at $\epsilon_l = -12.6\%$.

The change in sample cross-sectional area is quantified in Fig. 4a, and the corresponding increase in intergranular liquid fraction in Fig. 4b. The fraction liquid fluctuates due to variations in grain and dendrite morphology, with periodicities at both of these length scales. The distribution of local thickness of the liquid channels in the final stage of deformation was measured via a medial axis method [52] and plotted in the inserts of Fig. 4b. Fig. 5a and c compare the local thickness of the liquid channel in a central cube with an edge length of 1.47 mm (see black box in Fig. 4b)

at $\varepsilon_l = -1.2\%$ and the final deformation step ($\varepsilon_l = -12.6\%$). The intergranular channels are initially thin and highly tortuous (Fig. 5a), with regions thicker than $73\ \mu\text{m}$ only at the grain triple points (Fig. 5b). By the final stage of deformation (Fig. 5c), the liquid channel thickness has increased dramatically in the central region, with interconnected regions thicker than $73\ \mu\text{m}$ between almost all grains (Fig. 5d and quantitatively in Fig. 5e). This expansion of intergranular regions is an example of dilatancy, first described by Osborne Reynolds [55]. The grains were

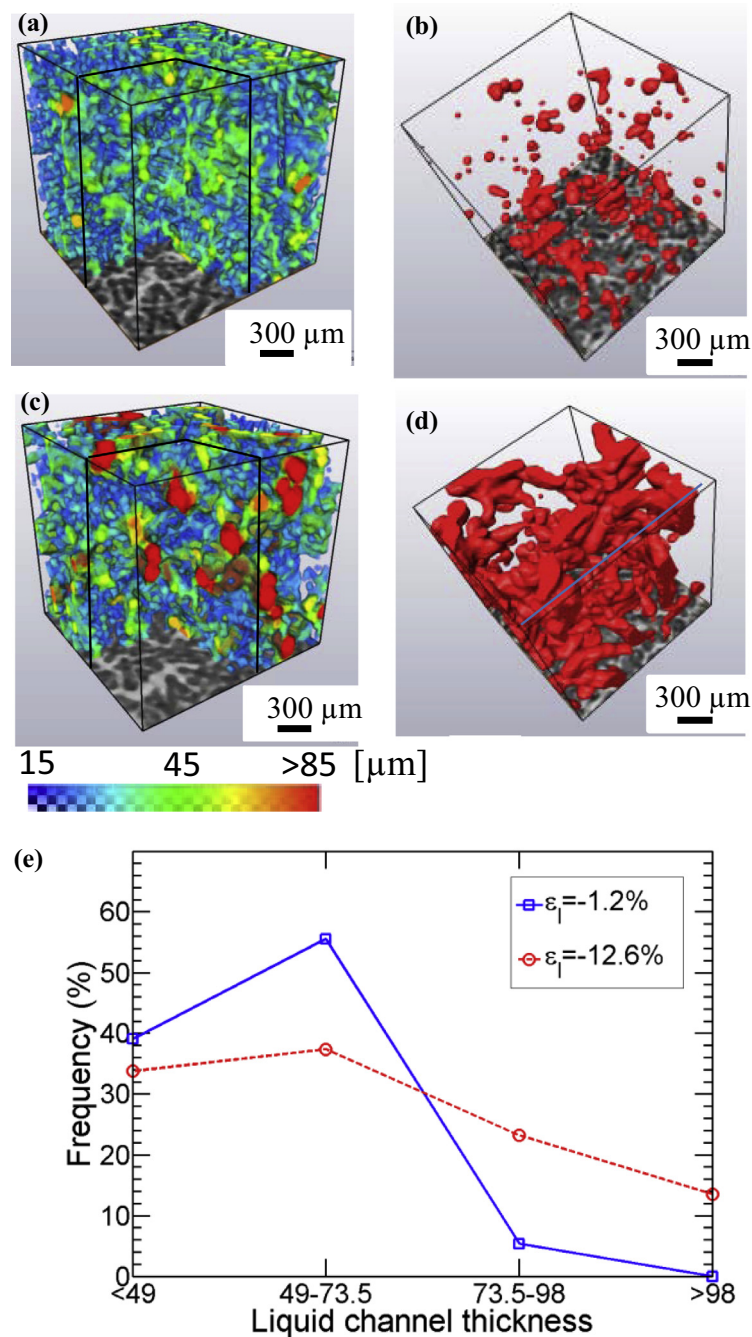


Fig. 5. (a, c) Liquid channel local thickness in central region for the subvolume box in Fig. 4 at $t = 24\text{ s}$ ($\varepsilon_l = -1.2\%$) and $t = 116\text{ s}$ ($\varepsilon_l = -12.6\%$), respectively. Liquid channels with local thickness larger than $73.5\ \mu\text{m}$ were rendered in (b) and (d); (f) distribution of the liquid channel thickness.

naturally packed initially, and when pushed, rearranged themselves to accommodate strain, widening the interstices in between.

We also observed another phenomenon that is less well reported. The dilation of the grains in the central region introduces a zone of low liquid pressure, which draws in interdendritic liquid from surrounding regions. In alloys this flow has an additional effect: it locally increases the average Cu concentration via mass transport, reducing the local equilibrium melting temperature, leading to local remelting of the solid grains. Although such remelting is best known in solute plumes/freckles due to thermal solute convection [56], observations in semi-solid tension via in situ X-ray radiography [57] and tomography [58] on Al–Cu alloys have indicated it can happen during

deformation. This local change in composition will further contribute to the increase in liquid fraction in the central, dilated region. Hence dilatancy in semi-solid alloys is different from that in insoluble soils, as localized changes in thermodynamic equilibrium may cause greater localization of shear banding. This effect may be significant in other fields such as volcanology, where an igneous magma is also a granular system that has a solid fraction that is dependent on local composition; deformation of a magma mass may cause the onset of dilation, producing zones of higher liquid fraction within the strain localized region [3] where remelting might also occur.

Dilatancy not only causes the increase of liquid volume fraction in the deformed region, but also leads to the formation of voids/damage (Figs. 2 and 6). (Note

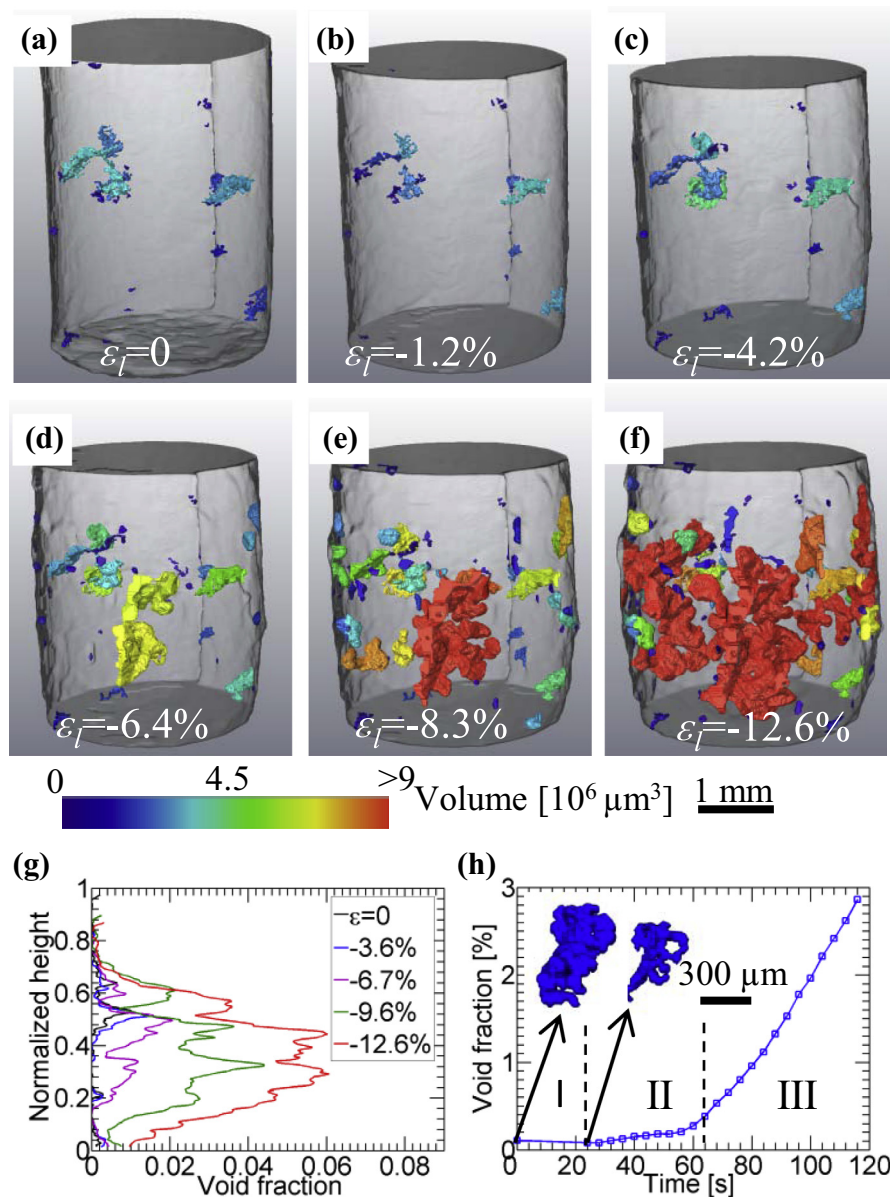


Fig. 6. (a)–(d) Evolution of voids (coloured according to its size) during semi-solid compression at $f_l \approx 30\%$ of a Al–15 wt.%Cu sample (transparent grey) at a deformation rate of $5 \mu\text{m s}^{-1}$ with an axis strain of (a) 0, (b) -4.2% , (c) -8.3% , (d) -12.6% . (e) Variation of void fraction in area along deformation axis. (f) Evolution of void fraction as a function of time (inserted images shows void closure at stage I).

we use the term damage interchangeably with voids, as the linkage of them leads to loss of mechanical integrity.) Three distinct stages of void evolution were identified in Fig. 6:

- I. Initial pore shrinkage;
- II. An incubation period; and
- III. Final rapid growth leading to cracking.

During stage I, the initial, 0.11% pre-existing porosity (Fig. 6a) shrinks as a result of both compressive strain and liquid feeding into the pore space (Fig. 6a and b, and one example is shown in Fig. 6h). Interestingly, Terzi et al. [47] also observed this during the initial stages of semi-solid tensile loading. During stage II, existing voids grow slightly along dendritic boundaries (Fig. 6b–d), and a few new ones are initiated. Two competing factors arise controlling the formation of voids in the mush zone: (i) tensile strain imposed on the liquid channel trying to open up a void; and (ii) the liquid feeding tending to feed the dilated space. Thus, when a critical amount of tensile strain is imposed on the liquid channels and the liquid fails to feed the dilated space, voids grow or are nucleated, resembling hot tear formation [57,59]. During the last stage (stage III), voids both rapidly grow and coalesce (starting at an axial strain of -6.4%), as seen in Fig. 6d–f. The damage penetrates into the sample (Fig. 6d), extending in the vertical direction (Fig. 6f and g).

Damage formation in a semi-solid depends on a balance between strain rate and fluid flow. At high strain rates, damage forms faster as liquid flow is insufficient to feed the newly dilated interdendritic space. The complex dendritic morphology and solid fraction also play a strong role as these control the interdendritic volume fraction and severity of dilatancy.

3.2. Bending and fragmentation of grains

Although dilatancy was the predominant mechanism for accommodating strain, other deformation mechanisms were also observed. Due to the irregular dendritic morphology, some grains interlocked, causing deformation within individual grains (termed intragranular deformation), specifically bending and fragmentation of the primary dendrite stems.

An example of this is shown in Fig. 7a–c; seven grains are labelled A–G to explain the breakage of C, bending of F and the associated force chain. When dendrite F is pushed down, its stem fragments near one tip (Fig. 7b). Load is transmitted to A and B from the grains above, pinning them against C, eventually shearing the dendritic stem of grain C (Fig. 7f and g). This breakoff may also have been added by local remelting, although the tomography resolution was insufficient to quantify this.

Looking now at grains E, F and G, a similar micro-mechanism is observed for F, leading to its eventual

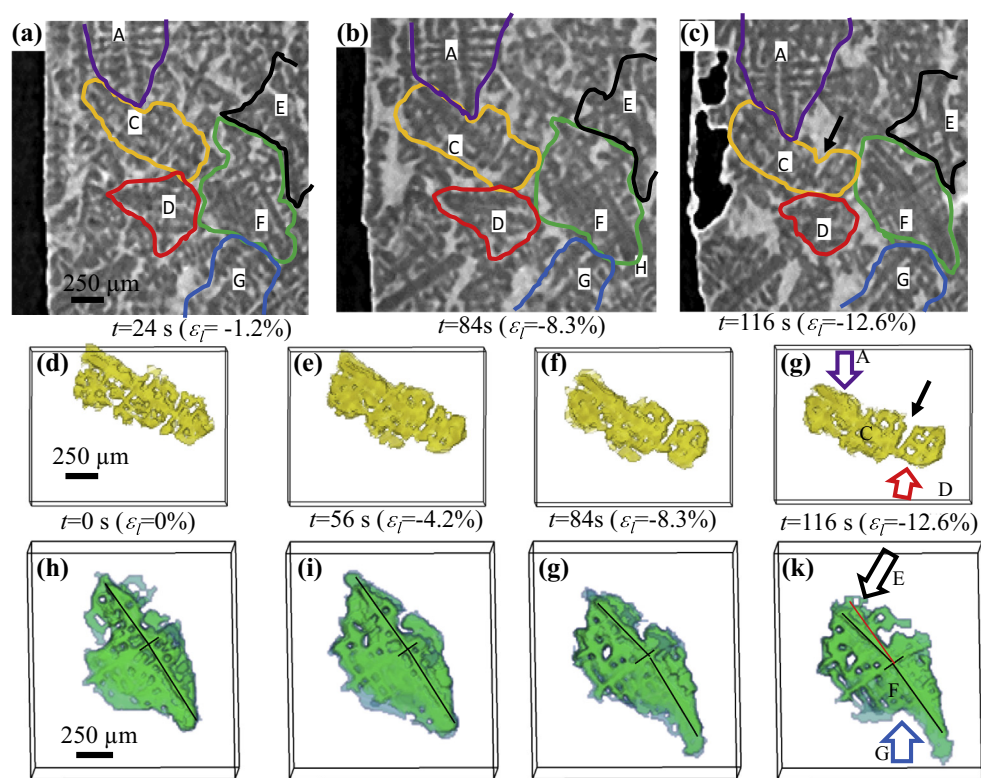


Fig. 7. (a)–(c) Zoomed longitudinal slice showing the bending and breakage of dendrites at time (a) 24 s, (b) 84 s, (c) 116 s; (d) 3-D rendering of α -Al grain marked “C” in images (a)–(c) at time 0 s, then at subsequent times (e)–(g) as the primary arm fragments due to loading from neighbouring grains to A and D. (h)–(k) 3-D rendering of α -Al grain F at subsequent times as the primary arm stem bends due to slow loading from neighbouring grains E and G.

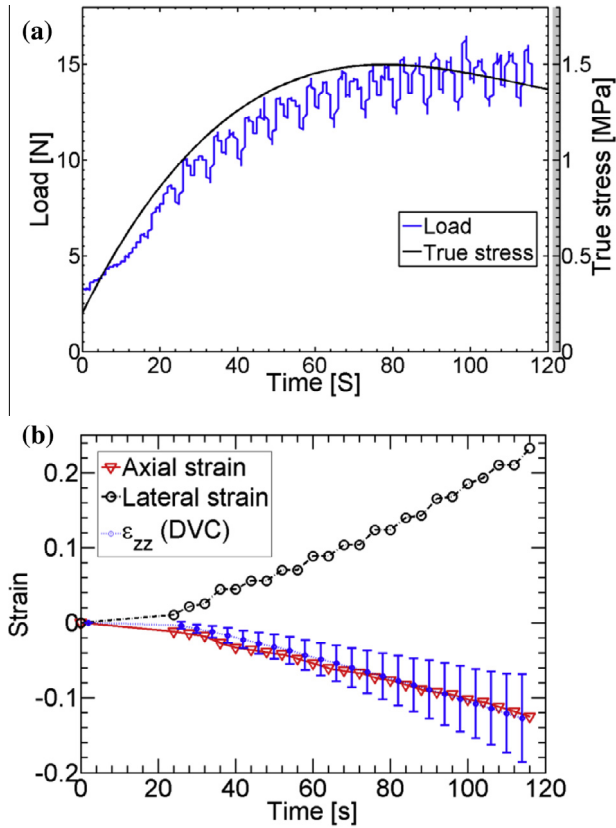


Fig. 8. (a) Load and true stress curve vs. time during semi-solid compression. (b) Axial strain, lateral strain and ϵ_{zz} vs. time.

bending. These grains also form a micro shear cell, where E and G tend to shear F in an anticlockwise direction (Fig. 7b). Under this configuration, the primary stem of grain F bends $\sim 15^\circ$ without breaking (Fig. 7k).

The current observations indicate that dendrites are sheared by their neighbours through a direct-shear mechanism; the shear force imposes a sufficiently high bending moment on the dendrite arms to bend and ultimately break

off portions of these equiaxed dendritic grains. Throughout the sample, many bent dendrites were observed, but break-off was less prevalent. Higher-resolution studies would be required to quantify the loads and stresses responsible for breaking individual dendrites.

For this particular solid fraction, dendritic morphology and strain rate, the predominant mechanisms, in order of prevalence, are: (i) dilatancy; (ii) grain deformation; and (iii) dendrite fragmentation. Granular models, particularly discrete element models of semi-solid materials, commonly consider the solid grains as rigid particles and treat particle–particle deformation as elastic deformation [14]. However, the present study suggests that the deformation of semi-solid equiaxed dendritic structures is considerably more complex.

3.3. Stress and strain measurement

In this section we correlate the granular flow behaviour and microstructural evolution to the measurement of the mechanical properties (stress and strain) during semi-solid deformation. During deformation, displacement and load values were recorded every millisecond (Fig. 8a). (Note the load fluctuates with the periodicity of sample rotation, required for tomography, due to slightly non-concentric loading; therefore, a weighted moving averaged load was used.) The resulting stress–time curve (Fig. 8a) has a maximum stress of ~ 1.4 MPa at 68 s (axial strain of -6.4%), corresponding to the initiation of rapid damage formation (stage II to stage III), slowly decreasing afterwards. The total work done on the sample is mainly consumed by: (i) grain rearrangement; (ii) deformation within grains; (iii) grain fragmentation; (iv) liquid flow through restricted channels; and (v) formation and growth of voids.

The axial and lateral strains vs. time (Fig. 8b) monotonically decrease and increase respectively during compression, as expected. The axial strain as calculated by DVC (ϵ_{zz}) is also plotted in Fig. 8b, correlating well with the

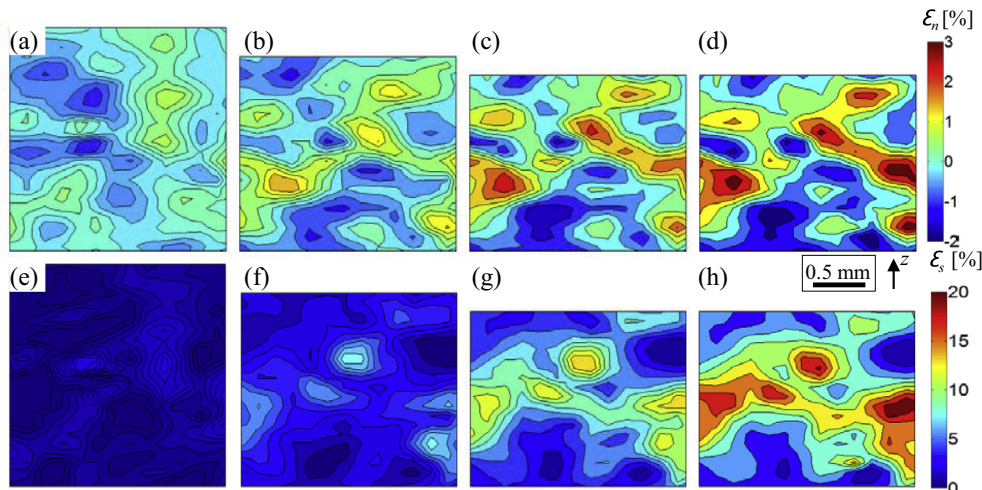


Fig. 9. (a)–(d) The development of octahedral normal strain; and (e)–(h) shear strain during semi-solid compression: (a) and (e) $\epsilon_t = 0$ –4.2%, (b) and (f) $\epsilon_t = 0$ –8.3%, (c) and (g) $\epsilon_t = 0$ –8.3%, (d) and (h) $\epsilon_t = 0$ –12.6%.

traditional measurement (ϵ_l). The increase in standard deviation of ϵ_{zz} indicates that the strain becomes more inhomogeneous during the course of the deformation, shown even more clearly by the DVC results (Fig. 9).

During the initial stages of deformation, the specimen predominantly exhibits relatively homogeneous negative normal strain, indicating compaction within the sample (Fig. 9a). As deformation progresses, positive normal strain (corresponding to dilation) occurs locally within the central region (Fig. 9b), accumulating with increasing deformation (Fig. 9c and d). The region with the highest positive normal strain ($>3\%$) is mainly located in the central region of the specimen (Fig. 9d). The octahedral shear strain tends to concentrate into a band (Fig. 9e–h), with the highest shear strain exceeding 12% (Fig. 9h). This suggests that the shear localization occurs as deformation increases, indicating the presence of dilatant shear bands.

In summary, the qualitative and quantitative analysis of this first 4-D in situ observation of an equiaxed dendritic semi-solid alloy during compression has not only highlighted the key mechanisms by which deformation occurs in semi-solids, but also shown how dilatancy gives rise to defect formation (shear bands and voids). The experimental methodology, techniques and analysis procedure used are generic in nature and can be applied to a wide range of cross-disciplinary research fields.

4. Conclusions

High-speed synchrotron X-ray tomographic microscopy was used to quantitatively analyze the compressive deformation of semi-solid equiaxed dendritic Al–15 wt.%Cu at $\sim 30\%$ liquid fraction. The results confirm the behaviour of this semi-solid structure as a granular system, highlighting how the deformation is accommodated not only by granular flow and associated dilatancy, but also by the formation of microshear cells resulting in intragranular bending and breakage of dendrites. These mechanisms lead to defect formation, causing segregation (which may cause local remelting, further increasing dilatant shear band formation), and damage formation, reducing mechanical strength. Three distinct stages of void evolution were identified: I, initial pore shrinkage; II, an incubation period with slow pore growth; and III, final rapid damage growth, both from the surface and via coalescence of internal and externally connected voids. These stages are directly linked to the granular behaviour of the solid phase. Using DVC, analysis of the full-field strain evolution showed regions of high strain concentrations corresponding to the formation of shear bands at a granular (microstructural) level.

Acknowledgments

This work was made possible by the facilities and support provided by the Research Complex at Harwell, funded in part by the EPSRC (EP/I02249X/1), EU (RFSR-PR-10005 DDT) and Diamond Manchester Collaboration (DMC).

The authors gratefully acknowledge the use of I12 beamline, Diamond Light Source (DLS) via EE7604-1 and the help provided by colleagues in DMC and DLS. B.C. acknowledges the University of Manchester, General Electric and China Scholarship Council for funding his Ph.D.

References

- [1] Fuloria D, Lee PD. *Acta Mater* 2009;57:5554.
- [2] Gourlay CM, Dahle A. *Nature* 2007;445:70.
- [3] Mead WJ. *J Geol* 1925;33:685.
- [4] Katz RF, Spiegelman M, Holtzman B. *Nature* 2006;442:676.
- [5] Flemings M. *Metall Mater Trans A* 1991;22:957.
- [6] Atwood RC, Sridhar S, Zhang W, Lee PD. *Acta Mater* 2000;48:405.
- [7] Dantzig J, Rappaz M. *Solidification: methods, microstructure and modeling*. EFPL Press; 2009.
- [8] Puncreobutr C, Lee PD, Hamilton RW, Cai B, Connolly T. *Metall Mater Trans A* 2012;44:5389.
- [9] Atkinson H. *Prog Mater Sci* 2005;50:341.
- [10] Ludwig O, Drezet J-M, Ménéès P, Martin CL, Suéry M. *Mater Sci Eng A* 2005;413–414:174.
- [11] Martin CL, Favier D, Suéry M. *Int J Plast* 1997;13:215.
- [12] Sistaninia M, Phillion AB, Drezet J-M, Rappaz M. *Acta Mater* 2012;60:6793.
- [13] Spencer DB, Mehrabian R, Flemings MC. *Metall Trans A* 1972;3:1972.
- [14] Yuan L, O'Sullivan C, Gourlay C. *Acta Mater* 2012;60:1334.
- [15] Phillion AB, Cockcroft SL, Lee PD. *Acta Mater* 2008;56:4328.
- [16] Tzimas E, Zavaliangos A. *Acta Mater* 1999;47:517.
- [17] Meylan B, Terzi S, Gourlay CM, Dahle AK. *Acta Mater* 2011;59:3091.
- [18] Nagira T, Yokota H, Morita S, Yasuda H, Yoshiya M, Gourlay CM, et al. *ISIJ Int* 2013;53:1195.
- [19] Gourlay CM, Nagira T, Dahle AK, Nakatsuka N, Uesugi K, Yasuda H. *IOP Conf Ser Mater Sci Eng* 2012;27:012086.
- [20] Zabler S, Ershov A, Rack A, Garcia-Moreno F, Baumbach T, Banhart J. *Acta Mater* 2013;61:1244.
- [21] Favier V, Atkinson HV. *Acta Mater* 2011;59:1271.
- [22] Ji S. *J Mater Sci* 2003;8:1559.
- [23] Yamaguchi M, Beckermann C. *Acta Mater* 2013;61:2268.
- [24] Farup I, Drezet J, Rappaz M. *Acta Mater* 2001;49:1261.
- [25] Phillion AB, Lee PD, Maire E, Cockcroft SL. *Metall Mater Trans A* 2008;39:2459.
- [26] Phillion AB, Cockcroft SL, Lee PD. *Scr Mater* 2006;55:489.
- [27] Ackermann P, Kurz W, Heinemann W. *Mater Sci Eng* 1985;75:79.
- [28] Fabrègue D, Deschamps A, Suéry M, Drezet JM. *Acta Mater* 2006;54:5209.
- [29] Colley LJ, Wells MA, Maijer DM. *Mater Sci Eng A* 2004;386:140.
- [30] Nguyen TG, Favier D, Suéry M. *Int J Plast* 1994;10:663.
- [31] Suéry M, Flemings MC. *Metall Mater Trans A* 1982;13:1809.
- [32] Kang CG, Choi JS, Kim KH. *J Mater Process Technol* 1999;88:159.
- [33] Sumitomo T, StJohn D, Steinberg T. *Mater Sci Eng A* 2000;289:18.
- [34] Martin CL, Brown SB, Favier D, Suéry M. *Mater Sci Eng A* 1995;202:13.
- [35] Bigot R, Favier V, Rouff C. *J Mater Process Technol* 2005;160:43.
- [36] Fonseca J, O'Sullivan C, Nagira T, Yasuda H, Gourlay CM. *Acta Mater* 2013;61:4169.
- [37] Meylan B, Terzi S, Gourlay CM, Suéry M, Dahle AK. *Scr Mater* 2010;63:1185.
- [38] Gourlay CM, Dahle AK, Nagira T, Nakatsuka N, Nogita K, Uesugi K, et al. *Acta Mater* 2011;59:4933.
- [39] Maire E, Withers PJ. *Int Mater Rev* 2013;59:1.
- [40] Wang Y, Liu X, Im K-S, Lee W-K, Wang J, Fezzaa K, et al. *Nat Phys* 2008;4:305.
- [41] Kureh KM, Lee PD, Gourlay CM. *IOP Conf Ser Mater Sci Eng* 2012;33:1.

- [42] Baker DR, Brun F, O'Shaughnessy C, Mancini L, Fife JL, Rivers M. *Nat Commun* 2012;3:1135.
- [43] Limodin N, Salvo L, Boller E, Suéry M, Felberbaum M, Gailliègue S, et al. *Acta Mater* 2009;57:2300.
- [44] Tolnai D, Townsend P, Requena G, Salvo L, Lendvai J, Degischer HP. *Acta Mater* 2012;60:2568.
- [45] Fife JL, Rappaz M, Pistone M, Celcer T, Mikuljan G, Stampanoni M. *J Synchrotron Radiat* 2012;19:352.
- [46] Suéry M, Terzi S, Mireux B, Salvo L, Adrien J, Maire E. *J Mater* 2012;64:83.
- [47] Sistaninia M, Terzi S, Phillion AB, Drezet J-M, Rappaz M. *Acta Mater* 2013;61:3831.
- [48] Jeng S-C, Chen S-W. *Acta Mater* 1997;45:4887.
- [49] Bhreasail ÁN, Lee PD, O'Sullivan C, Fenton CH, Hamilton R, Rockett P, et al. *Permafr Periglac Process* 2012;23:170.
- [50] Titarenko S, Withers PJ, Yagola A. *Appl Math Lett* 2010;23:1489.
- [51] Schneider CA, Rasband WS, Eliceiri KW. *Nat Methods* 2012;9:671.
- [52] Doube M, Klosowski MM, Arganda-Carreras I, Cordelières FP, Dougherty RP, Jackson JS, et al. *Bone* 2010;47:1076.
- [53] Mostafavi M, Baimpas N, Tarleton E, Atwood RC, McDonald SA, Korsunsky AM, et al. *Acta Mater* 2013;61:6276.
- [54] Rechenmacher AL. *J Mech Phys Solids* 2006;54:22.
- [55] Reynolds O. *Philos Mag J Sci* 1885;20:470.
- [56] Yuan L, Lee PD. *Acta Mater* 2012;60:4917.
- [57] Phillion AB, Hamilton RW, Fuloria D, Leung ACL, Rockett P, Connolly T, et al. *Acta Mater* 2011;59:1436.
- [58] Terzi S, Salvo L, Suéry M, Limodin N, Adrien J, Maire E, et al. *Scr Mater* 2009;61:449.
- [59] Rappaz M, Drezet J, Gremaud M. *Metall Mater Trans A* 1999;30:449.